Simplified procedure for the design and optimisation of oval tensile spoke wheels to be used in roof structures for sport stadiums

Rodrigo Martín-Sáiz[1]*, Blas Herrera[2]

[1]*Escola Tècnica Superior d'Arquitectura, Universitat Rovira i Virgili, Reus. Spain. Orcid: https://orcid.org/0000-0002-5232-3886*

[2]*Departament d'Enginyeria Informàtica I Matemàtiques, Universitat Rovira I Virgili, Tarragona, Spain. Orcid: https://orcid.org/0000-0003-2924-9195*

*Corresponding author: rodrigo.martin@urv.cat

Rodrigo Martín-Sáiz is an architect who obtained his Ph.D in Architecture at the Polytechnic University of Catalonia in 2015. Presently, he is an adjunct professor at the School of Architecture of the University Rovira i Virgili. His main field of research interest is the design of lightweight structures.

Blas Herrera is a Geometer who obtained his Sc.D in 1994. Presently, he is a full professor of Applied Mathematics –especially Applied Geometry– at the University Rovira i Virgili. His main fields of research interest are: Classical and Differential Geometry, and application of the Geometry to the Architecture and Engineering.

Simplified procedure for the design and optimisation of oval tensile spoke wheels for roof structures

This paper presents a simplified procedure for the design and shape optimisation of oval tensile spoke wheels to be used in roof structures for grandstands in sports stadiums. This procedure combines graphical methods with simple numerical methods to obtain the geometrical definition of an oval wheel and to estimate the prestressing forces. It also allows for the compression forces in the outer ring to be estimated and compared with those in a circular wheel. This makes it easy to make small geometrical adjustments for optimisation. Application examples are given for each step of the procedure. Several wheel designs are defined, showing how the shape of the inscribing oval determines the magnitude of the forces in the outer ring.

Keywords: Ovals, superellipses, tensile spoke wheels, graphic statics, roof structures.

1 Introduction

1.1 Ovals

Three ovals with two perpendicular axes of symmetry, formed by arcs of tangent circles, are considered (Figure 1). The simplest ovals of this type have four centres and four arcs with two different radii; they are commonly known as four-centered ovals and also as quadrarcs. The two centres of the arcs with the smaller radius lie on the x-axis line of the major axis, and the two centres of the arcs with the larger radius lie on the y-axis line of the minor axis. The next most complex ovals of this type have eight centres and eight arcs of three different radii, and are commonly known as eight-centered ovals. The geometric quality of the approximation of a given ellipse is higher using eight-centered ovals (with the arcs ordered from smallest to largest) than using four-centered ovals. A general and thorough discussion of this fact can be found in [1]. With the arcs

ordered from smallest to largest, the two centres of the arcs with the smaller radius lie on the x-axis line of the major axis, the two centres of the arcs with the larger radius lie on the y-axis line of the minor axis, and the four centers of the arcs with the intermediate radius lie outside of the two symmetry axes. On the other hand, if we take an oval with eight centres and place the four arcs with the smallest radius between the other arcs with the largest radius, we obtain a shape similar to a super-ellipse [2]. Therefore, in this oval, the two centres of the arcs with the larger radius lie on the y-axis line of the minor axis, the two centres of the arcs with the intermediate radius lie on the x-axis line of the major axis, and the four centres of the arcs with the smaller radius lie outside the symmetry axes.

The first quadrants of four-centered ovals are defined by equation (1), while the first quadrants of eight-centered ovals are defined by equation (2). In these equations, the parameters h_i, k_i are the coordinates (h_i, k_i) of the centres, r_i are the radii of each of the circle arcs and t_i are the abscissae of the tangency points, all in clockwise order starting from the arc closest to the y-axis.

$$y = \begin{cases} k_1 + \sqrt{r_1^2 - x^2}; 0 \le x < t_1 \\ \sqrt{r_2^2 - (x - h_2)^2}; t_1 \le x \le a \end{cases} \quad (1)$$

$$y = \begin{cases} k_1 + \sqrt{r_1^2 - x^2}; 0 \le x < t_1 \\ k_2 + \sqrt{r_2^2 - (x - h_2)^2}; t_1 \le x < t_2 \\ \sqrt{r_3^2 - (x - h_3)^2}; t_2 \le x \le a \end{cases} \quad (2)$$

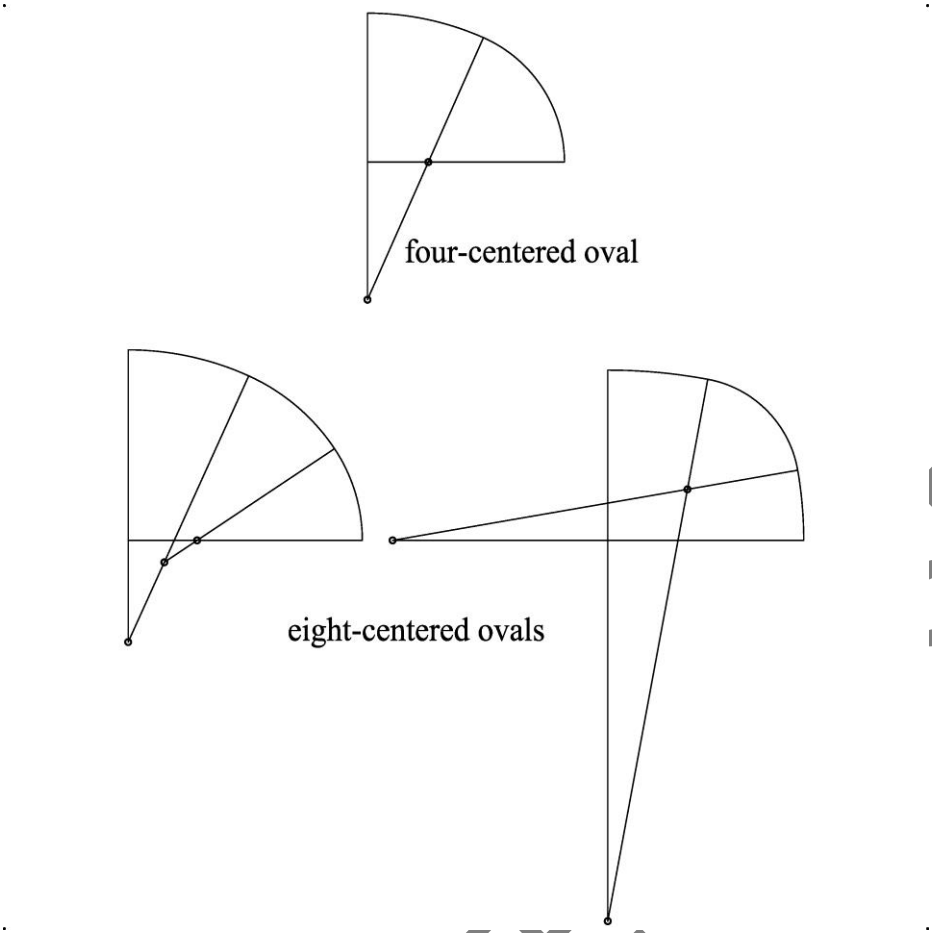

Figure 1: First quadrant of three ovals with two perpendicular symmetry axes.

1.2 The shape of sports stadiums

The outer perimeter of the stands in many sports stadiums is designed as a four-centered oval or an eight-centered oval. Four-centered oval shapes are typical for athletics arenas, for example the Olympic stadiums built for Rome 1960, Montreal 1976, Los Angeles 1984, Seoul 1988 and Athens 2004 [3]. Four-centered ovals can also be found in football stadiums, such as Maracana in Rio de Janeiro [4] or FC Krasnodar stadium in Russia [5]. Eight-centered ovals similar to ellipses are also typical for athletics arenas, for example the Olympic stadiums built for Berlin 1936 and London 2012 [3], or the Slaski Stadium in Silesia [6]. Eight-centered ovals similar to super-ellipses are typical for sports stadiums with a rectangular playing field, such as football, rugby or American football stadiums such as the Georgia Dome in Atlanta [7], the Allianz Arena

in Munich [8], the Commerzbank Arena in Frankfurt [9] or the Arena da Amazonia in Manaus [10]. Table 1 shows nine of the above-mentioned oval stadiums, sorted according to the type of oval.

4-centered ovals	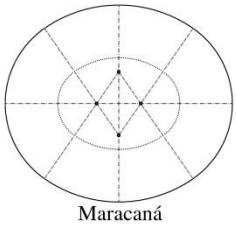 Maracaná	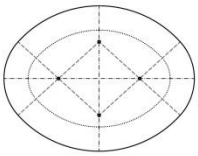 Montreal Olympic Stadium	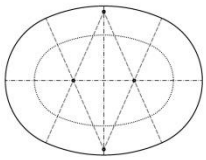 Athens Olympic Stadium
8-centered ovals like elipses	 Berlin Olympic Stadium	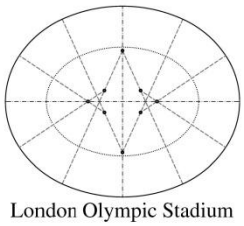 London Olympic Stadium	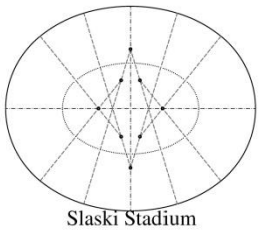 Slaski Stadium
8-centered ovals like superellipses	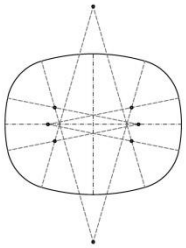 Georgia Dome	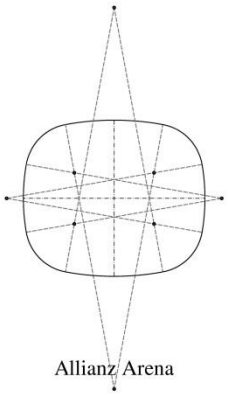 Allianz Arena	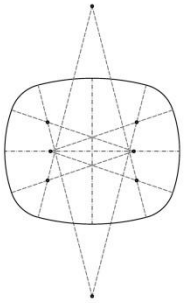 Commerzbank Arena

Table 1: Nine oval sports stadiums.

1.3 Tensile spoke wheels

The tensile spoke wheel (TSW) is probably the most widely used type of structure for grandstand roofs in large stadiums today. With overhangs longer than 35 m, TSWs are more efficient than any other type of structure [11]. The self-weight of overhanging steel girder or truss structures increases dramatically beyond 35 m. TSWs, on the other hand, are very light, even for very large spans, because they are mainly made of cables. In addition, TSWs do not transmit horizontal thrusts or bending moments. This

simplifies the design of the supports and their foundations, and also helps optimise their dimensions. Nonetheless, as will be described later in this paper, their efficiency depends on the shape of the oval in which they are inscribed. These structures are formed by tensile spokes which are connected to outer compression rings and inner tension rings. The number of compression and tension rings depends on the profile of the spokes (Figure 2): a biconvex or biconcave profile with one outer compression ring and two inner tension rings, or a biconcave profile with two outer compression rings and one inner tension ring [12].

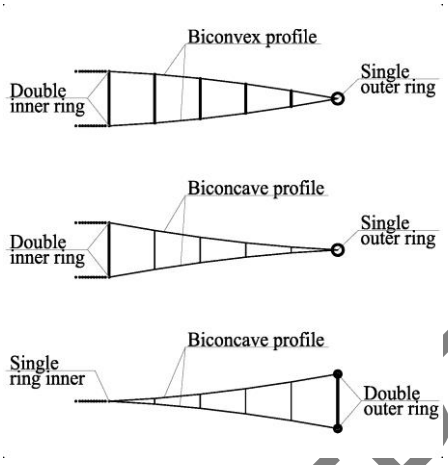

Figure 2: Spoke profiles and ring arrangement in TSWs.

Usually, the larger the stadium, the greater the number of spokes. This number determines the buckling length of the outer ring sections and the spacing between the spokes. If this spacing is too large, a secondary structure is required on which a membrane can be stretched.

The spokes consist of two wires, usually in the same vertical plane, separated by spacers. The number of spacers usually increases with the depth of the TSW, i.e. the overhang of the roof. The lower wire of the spoke with biconvex profile and the upper wire of the spoke with biconcave profile and double outer ring have the shape of a funicular polygon where the gravity loads are transferred from the inside to the outside

of the TSW, where the supports are located. These two profiles are therefore more suitable than the biconcave profile with single outer ring.

1.4 The outer ring as an optimisation goal

The outer rings concentrate the largest amount of material in TSWs. They are the largest elements and bear the highest compression forces. Therefore, any strategy to optimise the design of a TSW must aim to reduce these forces. Due to buckling, there is no linear relationship between the force and the size of the cross-section of the compressed ring. The greater the slenderness of the ring, the greater the influence of buckling on size. If there is only one compression ring, the compression force must be absorbed by a single cross-section, whereas if there are two compression rings, the same force is absorbed by two smaller cross-sections. Therefore, a single ring is usually less slender than a double ring. In this paper TSWs are considered with a single outer compression ring and a biconvex profile. It should be noted that spokes with a biconvex profile require bracing to avoid lateral instability.

The ideal design of a TSW inscribed in an oval is one in which, under permanent load (prestressing + self-weight), the shape of the outer ring coincides with the shape of the funicular polygon (a funicular polygon which has equal-length sides and is uniformly compressed) resulting from the tension forces on the spokes, which forces are projected on the ring plane. For equilibrium to exist, the shape of the inner ring must also coincide with the shape of a funicular polygon resulting from the same tension forces on the spokes, which forces are projected on the ring plane. Hereafter in this paper the rings will be referred to as the outer polygon and the inner polygon.

1.5 Simplified procedure for design and optimisation

The design and optimisation of an oval TSW is a non-linear problem the solution of

which is not trivial. Some recent procedures allow this problem to be approached in a precise way using iterative numerical methods, either generic [13-15] or specific to this type of structure [16-18], but their use is not straightforward and requires prior programming. Furthermore, the generic procedures usually do not aim at optimisation, but simply at finding an equilibrium shape. Other procedures based on graphic statics are simplified because they generally do not consider the effects of geometric non-linearity. 2D methods [19-23] are easy to use, but tend to only partially address the problem. 3D graphical methods [24-26] address the problem comprehensively, but can be complicated to use and require programming.

Against this background, this paper presents a simplified design and optimisation procedures for an oval TSW. This procedure approaches the problem comprehensively, combining simple iterative numerical methods with 2D graphical methods. Thus, architects or engineers can use it to obtain fairly optimised preliminary designs (which would need to be fine-tuned at a later stage using numerical methods to accurately solve the non-linear problem of large deformations typical of this type of structures) in a quick and simple way. The procedure presented here is only applicable to oval TSWs with two symmetry axes, where the spokes also have a symmetrical profile with respect to the plane of the outer polygon. The large deformations due to gravity loads are not considered, as they would alter the symmetry of the profile. The design steps are detailed below for the first quadrant of the wheel. This is sufficient because of the two perpendicular symmetry axes.

In addition to describing the design process, we present several graphs which relate the parameters defining the shape of the oval to the stress level of the outer polygon. In this way, we can make small geometric adjustments to the oval shape in

which the TSW is inscribed, allowing us to reduce the forces on the outer polygon and ultimately optimise the design.

2 Development

2.1 Parametric approximation of ovals by superellipses

A superellipse [2] is a certain type of closed line with variable curvature and two perpendicular symmetry axes. It is defined by an equation (3) which depends on three parameters: the semi-major axis *a*, the semi-minor axis *b* and the exponent *w*. The first two parameters determine the ratios. All three parameters determine the variation of the curvature.

$$\left(\frac{x}{a}\right)^w + \left(\frac{y}{b}\right)^w = 1 \tag{3}$$

The original oval is defined by equation (1) or (2). Now, let us consider an approximating superellipse. This superellipse must have the same semi-axes $\{a, b\}$. Furthermore, the superellipse and the oval must coincide at the intermediate point *W*, which is located at the intersection with the diagonal of the rectangle inscribing the quadrant of the oval. This superellipse is defined by its parameter *w*, which is given by the following equation (4):

$$w = \frac{\ln 2}{\ln \frac{D}{R}} \tag{4}$$

where *D* is the length of the diagonal and *R* is the distance from the origin of the coordinate system to point *W* (see Figure 3 left). This equation (4) was found along the following line of reasoning: Equation (3) in polar coordinates is

$(\rho\cos\theta/a)^w+(\rho\sin\theta/b)^w=1$. The polar coordinates of point *W* are

$\theta=\arccos(a/D)$ and $\rho=R$; hence: $(Ra/D/a)^w+(Ra/D/b)^w=1\Rightarrow$

$R^w\,2/D^w=1\Rightarrow R^w=D^W/2\Rightarrow \ln R^w=\ln(D^w/2)\Rightarrow w\ln R=w\ln D-\ln 2\Rightarrow$
$w(\ln R-\ln D)=-\ln 2\Rightarrow w=\ln 2/\ln(D/R)$.

Thus, approximating superellipses were defined for the three ovals of types of the Figure 1 which were used in the design of two Olympic stadiums —those built for Athens 2004 (*a*=130 m; *b*=98,5 m; *w*=2,177) and London 2012 (*a*=154,7 m; *b*=125,9 m; *w*=2,045)— and the Allianz Arena football stadium in Munich (*a*=129,5 m; *b*=112,5 m; *w*=2,952). Figure 3 shows the three original ovals (in green) and the three approximating superellipses (in red). Parameters *D*, *R* and *W* used in our calculations are shown on the first oval. The reader can see how little difference there is between them. The maximum radial relative approximation error of the superellipse with respect to the oval is defined by the equation $\varepsilon_{max}=\max_x\left|1-\left(\sqrt{x^2+y_s^2}/\sqrt{x^2+y_o^2}\right)\right|$, where (x,y_s) and (x,y_o) are the coordinates of the points of the superellipse and the oval, respectively. This error is 0.0073 for the Athens Stadium, 0.0019 for the London Stadium and 0.0109 for the Munich Stadium.

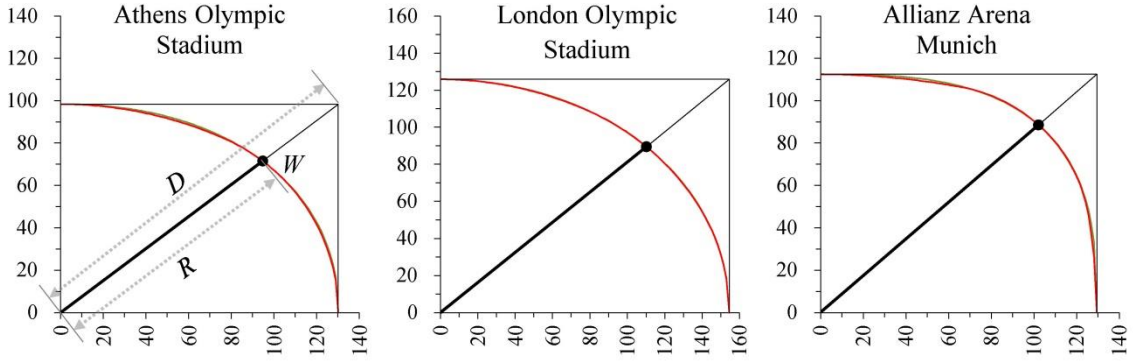

Figure 3: Superellipses (in red) approximating the ovals (in green) of three sports stadiums

2.2 The outer polygon

A polygon with 4*n* equal sides inscribed in a superellipse is defined (figure 4). The ends of the polygon quadrant coincide with the midpoint of the endmost sides. For this reason, the maximum dimensions of the polygon are slightly smaller than those of the superellipse.

The length of the middle sides is defined by equation (5). The length of the endmost sides is given by equations (6) and (7). The coordinates of the midpoint of the endmost half-sides are (0, y_n) and (x_1, 0). The coordinates of the remaining vertices of the first quadrant are defined by equation (3), in which we add a subindex *i* to the variables *x* and *y*, where $i = 1 \div n$.

$$c = \sqrt{\left(x_{i+1} - x_i\right)^2 + \left(y_{i+1} - y_i\right)^2}; i = 1 \div n-1 \tag{5}$$

$$c = 2x_1 \tag{6}$$

$$c = 2y_n \tag{7}$$

Thus, a nonlinear system of $2n+1$ equations (3, 5-7) is obtained in which the variables are *c* and (x_i, y_i) with $i = 1 \div n$. Throughout this paper, the notation $i = A \div B$ indicates that *i* varies between *A* and *B* with the stated increment value, or with an increment value of 1 if not stated. To solve this system of equations, an iterative numerical method is proposed which has already been used in previous investigations [18]. This method is briefly summarised below: A notation with two subindexes is used: the first subindex refers to the number of the polygon side and the second subindex refers to the number of the iteration. A starting point is defined such that the coordinates x_i of the vertices are $x_{i,0} = a\cos\left(\left(\pi/2\right)\left(i-1/2\right)/n\right)$ where $i = 1 \div n$. Next, $x_{i,0}$ is replaced in equation (3),

obtaining $y_{i,0}$. Next, $\lambda_{i,0} = c_{i,0} \Big/ \left(\sum_{i=1}^{n} c_{i,0} \Big/ n \right)$ is calculated, where

$c_{i,0} = \sqrt{\left(x_{i+1,0} - x_{i,0} \right)^2 + \left(x_{i+1,0} - x_{i,0} \right)^2}$. The abscissa value of each vertex is modified according to equation $x_{i+1,j+1} - x_{i,j+1} = \left(x_{i+1,j} - x_{i,j} \right) \Big/ \lambda_{i,j}$, so that the new $y_{i,j+1}$, $c_{i,j+1}$ and $\lambda_{i,j+1}$ are found. This process is repeated in successive iterations until the ratio $\lambda_{i,j+1}$ is close to 1 with an error $\varepsilon_i = \left| 1 - \lambda_{i,j+1} \right| \leq 10^{-3}, i = 1 \div n$.

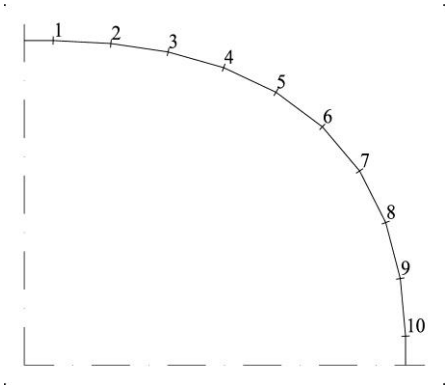

Figure 4: Numbering of the vertices of the first quadrant of a polygon with equal sides and n=10 which is inscribed in a superellipse.

Table 2 shows the ratio c/a of the polygons with n=10 which are inscribed in 104 different superellipses with $b/a = 0.65 \div 1$ (increment value of 0.05) and with $w = 2 \div 3$ (increment value of 0.1, besides w=2.25 and w=2.75). This makes it possible to easily define an inscribed polygon with 40 equal sides without having to use the iterative numerical process described above.

b/a	**0.65**	**0.70**	**0.75**	**0.80**	**0.85**	**0.90**	**0.95**	**1.00**
W	***c/a***							
3.00	0.1398565	0.1437968	0.1477892	0.1518290	0.1559122	0.1600352	0.1641949	0.1683885
2.90	0.1391673	0.1430758	0.1470383	0.1510500	0.1551066	0.1592046	0.1633405	0.1675116
2.80	0.1384402	0.1423151	0.1462459	0.1502278	0.1542563	0.1583277	0.1624385	0.1665859
2.75	0.1380616	0.1419189	0.1458332	0.1497994	0.1538133	0.1578708	0.1619685	0.1661035
2.70	0.1376725	0.1415116	0.1454088	0.1493591	0.1533578	0.1574010	0.1614853	0.1656075
2.60	0.1368611	0.1406622	0.1445237	0.1484403	0.1524074	0.1564208	0.1604769	0.1645725
2.50	0.1360030	0.1397635	0.1435870	0.1474679	0.1514013	0.1553830	0.1594093	0.1634767

2.40	0.1350947	0.1388120	0.1425949	0.1464377	0.1503353	0.1542834	0.1582779	0.1623154
2.30	0.1341328	0.1378038	0.1415434	0.1453455	0.1492051	0.1531173	0.1570781	0.1610839
2.25	0.1336306	0.1372773	0.1409941	0.1447749	0.1486144	0.1525079	0.1564511	0.1604403
2.20	0.1331136	0.1367351	0.1404284	0.1441872	0.1480061	0.1518801	0.1558051	0.1597772
2.10	0.1320332	0.1356019	0.1392457	0.1429582	0.1467337	0.1505671	0.1544540	0.1583903
2.00	0.1308879	0.1344002	0.1379912	0.1416543	0.1453835	0.1491736	0.1530199	0.1569182

Table 2: Ratio *c/a* for polygons of 40 equal sides which are inscribed in superellipses.

2.3 The inner polygon and the in-plane distribution of forces

Graphic statics is an accurate form finding tool for structures, but it does not allow consideration of geometric non-linearity effects due to large deformations. A TSW undergoes large deformations in its own plane, and we want these deformations to be homothetic. Thus, although the deformation is large in absolute terms, the plan shape of the TSW does not change. It undergoes a reduction in size that is directly proportional to the magnitude of the compression force on the outer polygon. In other words, its in-plane behaviour is linear.

We will use graphic statics techniques in order to find the tension forces on the spokes. These forces are projected on the wheel plane and result in a known funicular polygon, the shape of which was found in the previous section. This polygon has equal-length sides and is uniformly compressed.

Figure 5 shows the graphic statics method used to obtain the spokes arrangement and the in-plane distribution of tension forces for a TSW which is inscribed in a superellipse. This method is described below.

Given an outer polygon with 4*n* equal sides and a uniform compression force of value N=1, n concurrent segments of length 1 are highlighted in red. The angle α_i between the x-axis and each segment is the same angle that the x-axis forms with each of the sides of the outer polygon in the plan view. Next, all the ends opposite the point of concurrence are joined. The result is a polygonal line (highlighted in blue), the sides

of which represent the tension forces F_i on the spokes. These forces are projected on the outer polygon plane and generate a funicular polygon (the outer polygon) which is subject to a compression force N=1. In actual fact, this is a way to determine F_i/N, i.e., the relative distribution of these forces in each TSW. Next, these tension forces are plotted on the vertices of the outer polygon of each TSW. The angle φ_i of these tension forces coincides exactly with that of the bisector of the angle formed by the sides of the outer polygon at each vertex. Finally, in order to define the inner polygon, the bisector closest to the X axis is extended until it intersects the line $x=d$, where d is the depth of the TSW or, in other words, the overhang of the roof. From this first point, the inner polygon is drawn. The sides of this inner polygon are parallel to those of the outer polygon, and its vertices lie at the same bisectors. This provides the shape and the distribution of the tension forces on the plane of the TSW. The outer and inner polygons are affine funicular polygons resulting from the same forces. The shape and the in-plane distribution of forces are scalable, both in dimensions and in the magnitude of the forces, i.e., they are valid for any value of N and any size of TSW having the same shape.

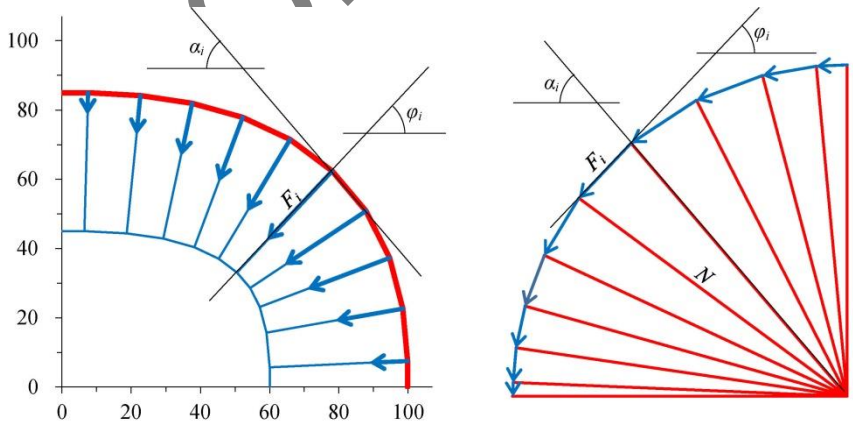

Figure 5: Graphic statics method used to obtain the spokes arrangement and the in-plane distribution of tension forces for a TSW which is inscribed in a superellipse.

Table 3 shows the spokes arrangement and the in-plane distribution of forces for fifteen $n=10$ TSWs which are inscribed in superellipses with $a=100$ m, $b=70\div100$ m (increment value 15) and $w=2\div3$ (increment value 0.25).

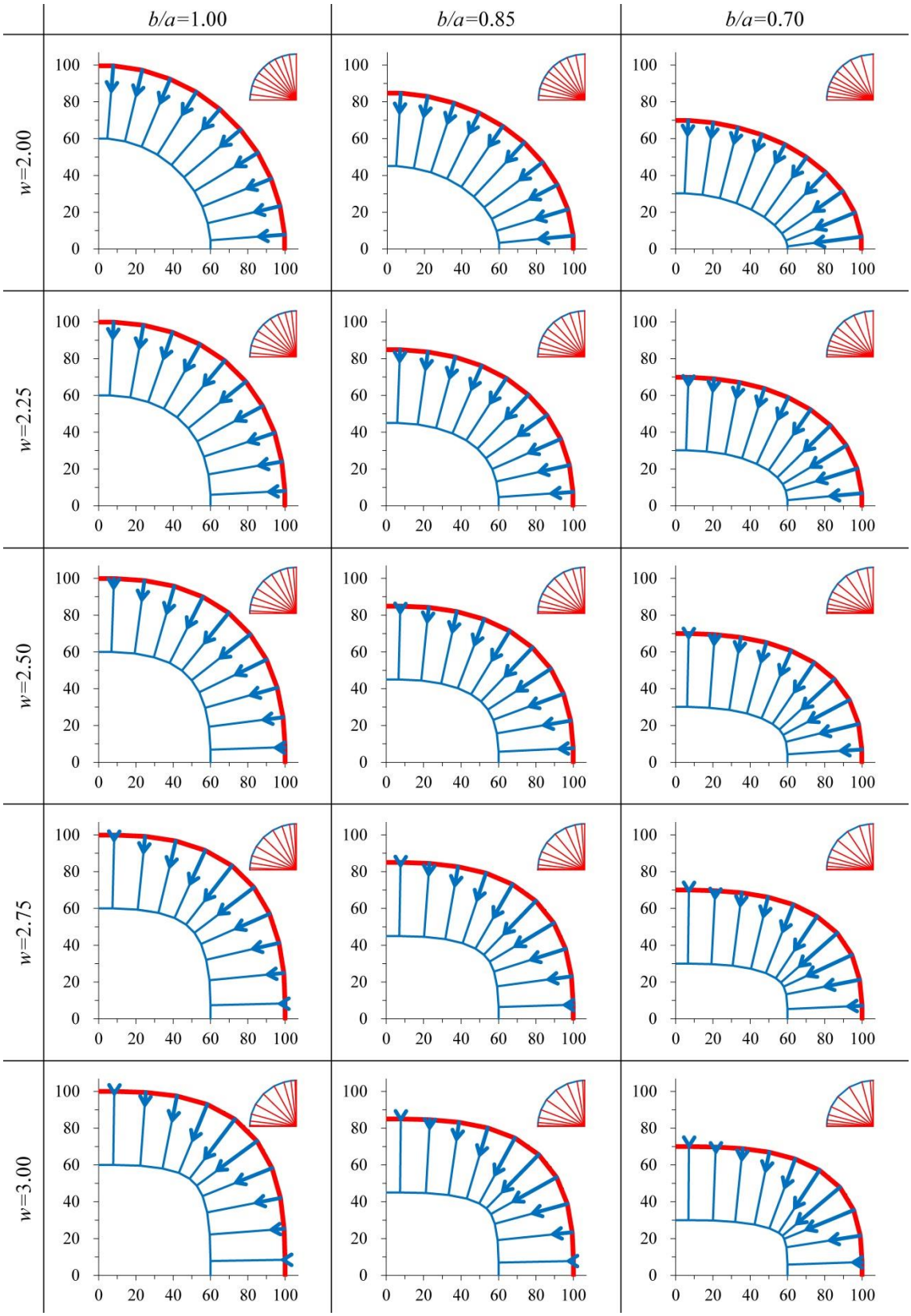

Table 3: Spokes arrangement and in-plane distribution of tension forces for fifteen n=10 TSWs which are inscribed in different superellipses. Results obtained using graphic statics techniques.

2.4 Preliminary sizing

We assume a maximum value of surface load $\pm q_{max}$ (upward and downward load), corresponding to the worst possible load combination in each direction. We then use equation (8) to calculate the bending moment M_n produced by these loads at the inner end (coinciding with the inner rings) of the spoke closest to the *Y* axis (the minor axis of the super-ellipse), as this spoke supports a larger roof area:

$$M_n = \frac{(2r_n)^2}{8}\left(q_1 + \frac{q_2 - q_1}{3}\right) \quad (8)$$

where r_n is the length of the spoke closest to the Y-axis, and q_1 and q_2 are the values of the distributed linear load. These values are calculated for each spoke based on $\pm q_{max}$, according to Figure 4.

Next, M_n is decomposed into a pair of horizontal forces $\pm H_n$, separated by a distance equal to the length $h_n = d/4$ of the mast at the inner end of this spoke. Then, a prestressing force is introduced so that the lower and upper wires remain tensioned in any load situation, taking into account a safety margin of $1/\gamma_G$. If we take Eurocode 0: 'Basis of structural design' as a reference, table A1.2(A) 'Design values of actions' in Annex A1 'Application for buildings' [27] defines a partial factor γ_G=0.9 for permanent actions, such as prestressing, if their effects are favourable. Thus, the reaction forces $H_{n,\max}$, $H_{n,\min}$, F_n and V_n shown in Figure 6 are calculated with the equations (9a-9d).

$$H_{n,\max} = \frac{F_n}{2} + \frac{M_n}{h_n}; H_{n,\min} = \frac{F_n}{2} - \frac{M_n}{h_n}$$
$$F_n = \frac{2M_n}{\gamma_G h_n}; V_n = r_n\left(q_1 + \frac{q_2 - q_1}{2}\right) \quad (9a, 9b, 9c y 9d)$$

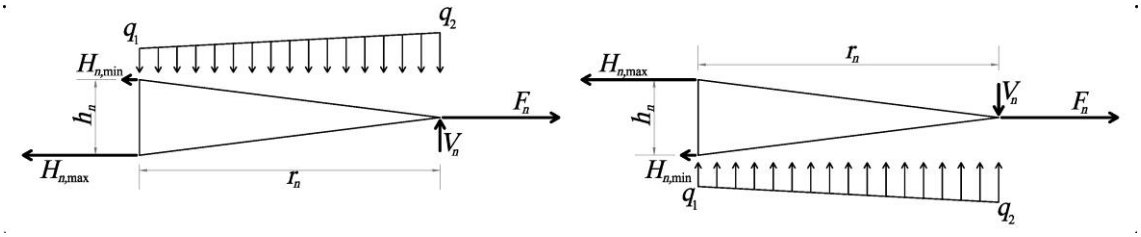

Figure 6: Schematic of the reaction forces at the ends of a spoke for maximum upward and downward loads.

Based on F_n and the F_i/N ratio obtained in the previous section using graphic statics techniques, we calculate the values of $F_{i,\max}$ and F_i for the remaining spokes, and also the value of N at the outer polygon. Then, the h_i length is calculated for the remaining masts between the inner polygons, using the equation (10a) if $F_{i,\max} \leq 2F_n$, or using the equation (10b) if $F_{i,\max} > 2F_n$:

$$h_i = \frac{h_n F_n}{F_i}; h_i = h_n\left(1 - \left(\frac{\left(F_{i,\max} - F_i\right)}{2\left(F_{i,\max} - F_n\right)}\right)\right) \qquad \text{(10a and 10b)}$$

The length of the masts resulting from equation (10a) is inversely proportional to the value of the force *Fi* on each spoke. As a result, the tension forces on the cables are very similar for all the spokes. If $F_{i,\max}$ is more than twice as large as F_n, in order to avoid very large differences between the longest masts of each spoke, which would also lead to large differences in their stiffness, we can use equation (10b) to obtain a value for the length of the longest mast of each spoke by weighting the proportionality with a limit of 2 in the difference between $h_{i,\max}$ and $h_{i,\min}$.

Based on the reaction forces $P_{i,\max}$ at the ends of the spokes, we can obtain the estimated maximum stresses on the wires of the spokes and the inner polygons, as well as on the longest masts. Finally, a preliminary dimensioning estimate can be made for all the elements of the TSW, with the exception of the intermediate masts, the definition

of which will be discussed in the next section. Hollow, tubular or box sections of steel, reinforced concrete or steel-concrete composite can be used for the outer polygon. Hollow tubular steel or solid timber sections can be used for the masts. High strength steel or carbon fibre reinforced polymer (CFRP) bars or cables can be used for the spoke wires and for the inner polygons [28-30]. Alternatively, other more sophisticated preliminary sizing methods can be used [31].

2.5 Profile of the spokes

We consider the funicular polygon resulting from the permanent loads gravitating on the bottom wire of each spoke. To find the precise shape of this funicular polygon it would be necessary to solve a geometric nonlinearity problem, using iterative numerical methods [32, 33] and taking into account the elongations produced in each wire span, as well as the prestressing force. If we dispense with both and use graphic statics techniques, we can find a funicular polygon of inextensible sides which is very similar to the precise shape we would find by means of a non-linear calculation using iterative numerical methods. This funicular polygon is determined by the number of masts, the maximum deflection, i.e. $h_i/2$, and the magnitude of the permanent gravity loads. These loads are the sum of the self-weight of the cables, the masts, and a roof membrane, as well as other bracing elements.

Therefore, the following steps are taken. We start with an initial profile in the form of an isosceles triangle, as shown in Figure 4. We place evenly spaced intermediate masts within this triangle. We calculate the dead weight of all the cables and masts according to their length in this first figure, their material and their cross-section. To estimate the cross section of the intermediate masts, it is now sufficient to limit their slenderness (λ) according to $\lambda \simeq 100$. We add the weight of the membrane and the bracings according to the roof area loaded on each mast. Then, using graphic

statics techniques, we define the funicular polygon of the forces resulting from these loads (Figure 7). The position of the ends of this polygon is known. We also know that the resultant force at the inner end is horizontal.

Once the shape of the lower wire has been determined, we use symmetry to determine the shape of the upper wire and thus the height of all the intermediate masts. The final length of the wires and masts is slightly greater than the initial length assumed with the isosceles triangle, but in general it will not be necessary to recalculate the self-weight loads and repeat the graphic statics procedure. The polygon resulting from a re-adjustment of the loads would be little different from the one we have already found. Finally, also using graphic statics techniques, we find the tension forces on the cables and on the spoke masts.

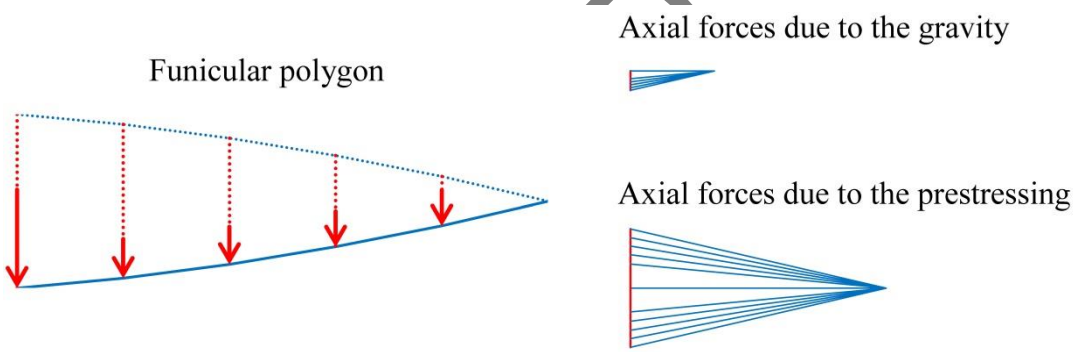

Figure 7: Graphic statics to determine the tension forces and the shape of the funicular polygon resulting from permanent gravity loads on a spoke with five masts and biconvex profile.

Table 4 shows the longitudinal profile of fifteen TSWs with the plan design outlined in Table 3. In order to define the length h_i of the longest masts of each spoke, we have used equation (10a) or (10b), as appropriate, with $h_n = d/4$. We find that the profile of the spokes of the TSWs inscribed in superellipses with w close to 2 has a lenticular shape, while the profile of the spokes of the TSWs inscribed in superellipses with w close to 3 has a shape similar to an isosceles triangle. In the former TSWs, the tension

force on the inner polygon is reduced, so that the weight of the wires is not concentrated at the inner end, but is more evenly distributed along the entire spoke. Conversely, in the latter TSWs, the tension force on the inner polygon is very high in relation to the tension force on the spokes, which means that the weight of the cables is concentrated at the inner end. This difference in load distribution, which in turn is due to the difference in tensions on the inner polygons, is apparent in the shape of the funicular polygon that makes up the profile of the spokes.

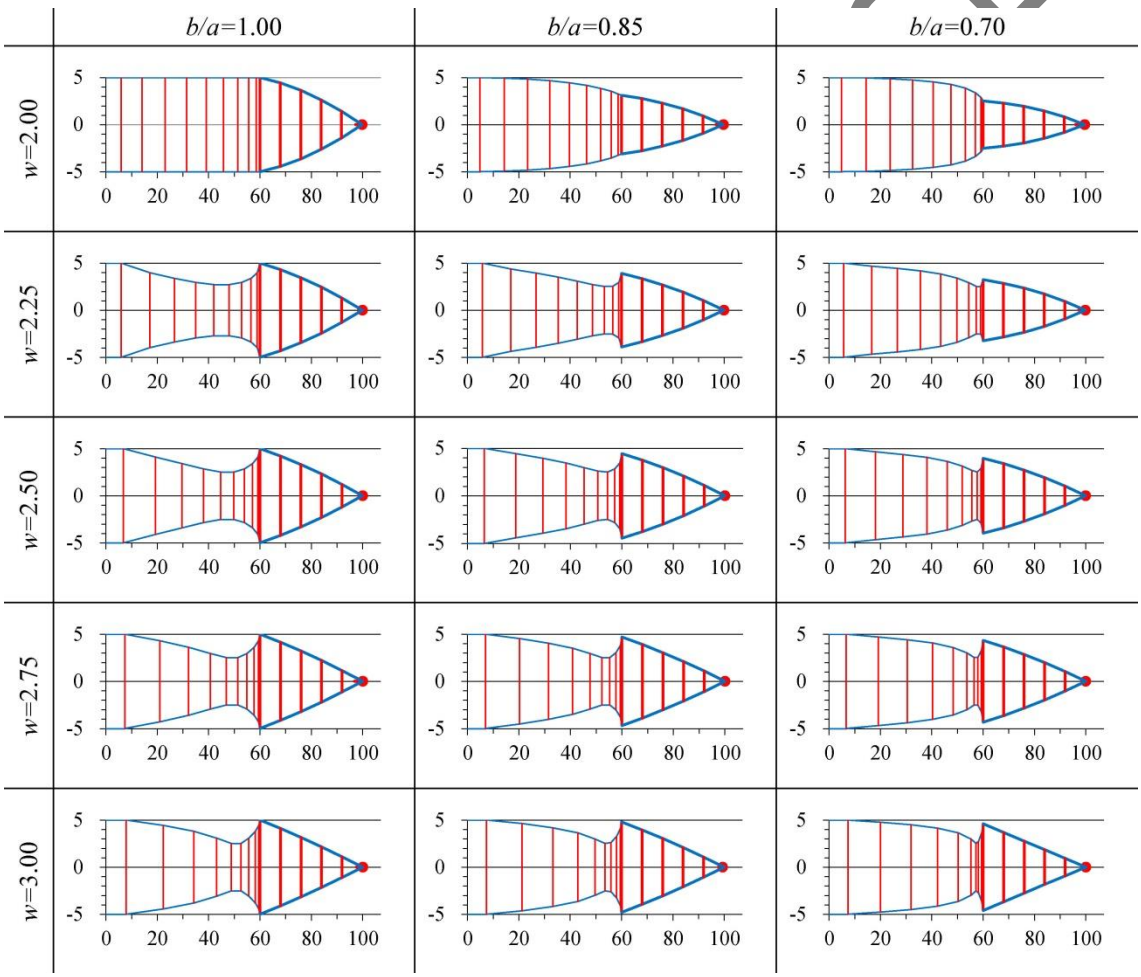

Table 4: Longitudinal profile of fifteen TSWs with n=10 which are inscribed in different superellipses.

2.6 Optimization

Using the procedure described in the previous sections, we obtained the design of 412

TSWs with n=10 which are inscribed in superellipses with a=100 m, $b = 65 \div 100$ m (increment value 15), $w = 2 \div 3$ (increment value 0.1, adding also w=2.25 and w=2.75), and $d = 35 \div 50$ m (increment value 5). The compression force (N) on the outer polygon of each TSW was estimated assuming $q_{max} = \pm 1$ KN/m^2. The results are shown in the four graphs in Figure 6 for d=0.35a, d=0.40a, d=0.45a and d=0.50a respectively. The horizontal axis represents the ratio b/a, while the vertical axis represents the ratio N/N_O, where N_O is the compression force that a TSW which is inscribed in a circle would have. Each graph shows the curves with the results obtained for each w value. The coordinate (1,1) corresponds to a TSW inscribed in a circle. In this way, it is possible to estimate how the compression force on the outer polygon of the TSW would increase as the shape of the superellipse in which it is inscribed moves away from the circumference. According to these curves, this increase is much more pronounced when the exponent w varies than when the ratio b/a varies, and is only slightly modified when d changes. For example, the outer polygon of a TSW with d=0.40a inscribed in an ellipse with b/a=0.65 would have a compression force approximately 1.75 times greater than that of a TSW inscribed in a circle, while the outer polygon of a TSW inscribed in a superellipse with b/a=1.00 and w=3 would have a compression force almost seven times greater.

The graphs in Table 5 can then be used to predict the behaviour of a TSW without having to solve its design in its entirety, based on a) the parameters $\{a,b,w\}$ which define the superellipse approximating the inscribing oval, and b) the depth d. Thus, small geometric adjustments can be made to the oval in order to reduce the compression force on the outer polygon. For example, the outer perimeter of the stands of the Commerzbank Arena in Frankfurt is an eight-centered oval with three different radii. The approximation superellipse, calculated according to equation (4), has the

following parameters: a=115.75 m, b=96.40 m, b/a=0.833, and w=3.022. When designing the TSW for the roof structure of this stadium, the firm Schlaich Bergermann Partner Engineering slightly modified the shape of the oval inscribing the outer polygon *"... to create a viable structural system with moderate forces"*. [9] The superellipse approximating this second oval has the following parameters: a=119.28 m, b=100 m, b/a=0.838 and w=2.360. Figure 7 shows the first quadrant of these two superellipses. The superellipse outlining the stands perimeter is shown in purple, and the superellipse outlining the TSW which forms the roof structure is shown in orange. Figure 8 also shows the design and in-plane radial force distribution for two n=10 TSWs inscribed in these two superellipses. These superellipses are also plotted on the fourth graph in Table 5. It can be seen that, for a TSW inscribed in the first superellipse, the value of N/N_O would be slightly higher than the value obtained for w=3, whereas for a TSW inscribed in the second superellipse, the value of N/N_O would lie between the values obtained for w=2.30 and w=2.40. In other words, this small geometric adjustment of the TSW perimeter allowed a reduction of approximately 70% of the compression forces on the outer polygon and, consequently, a significant optimisation of the amount of material used in the roof structure.

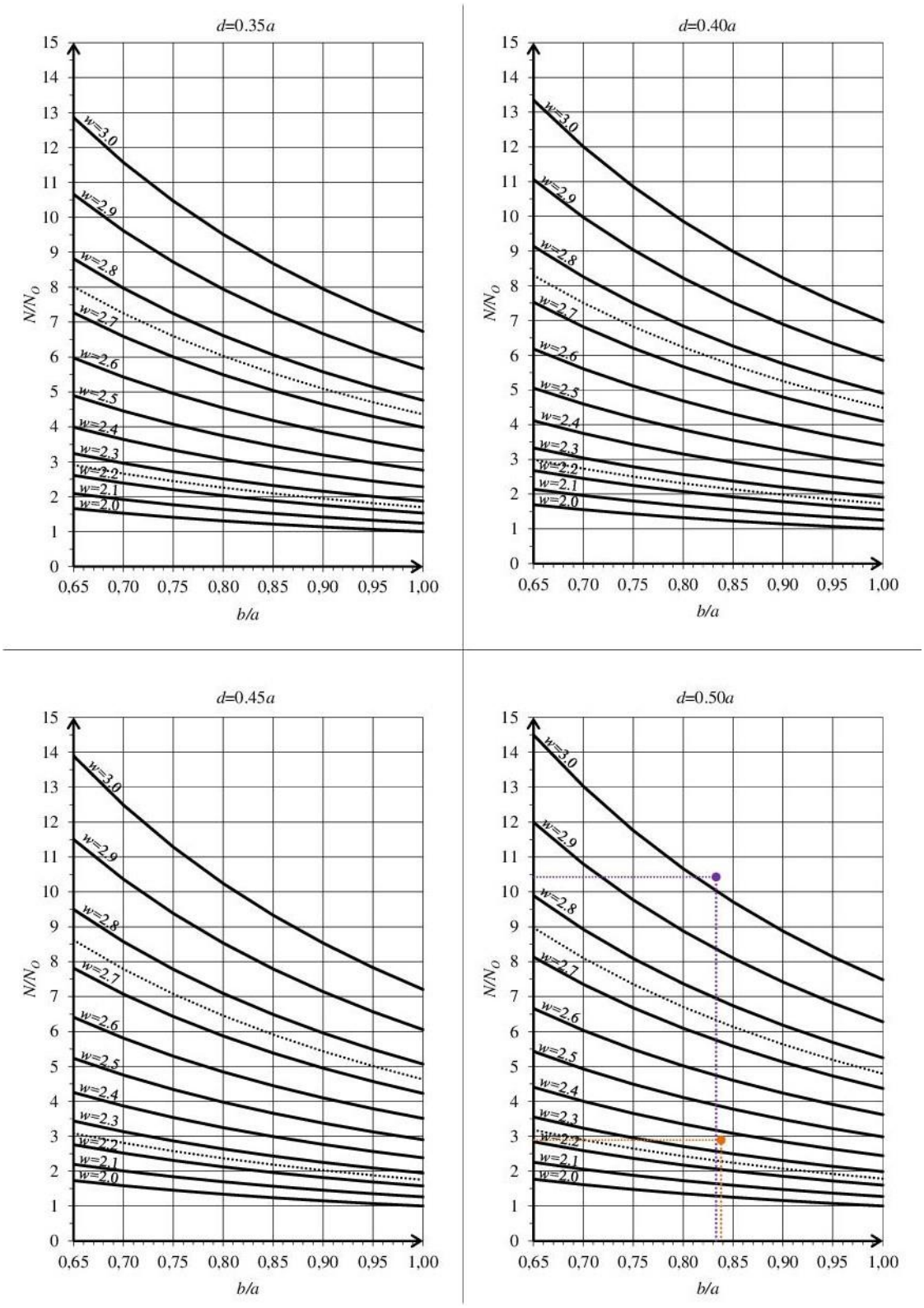

Table 5: Variation of N/N_O at the outer polygon of a n=10 TSW as a function of the shape of the inscribing superellipse and of depth, for d=0.35a, d=0.40a, d=0.45a and d=0.50a.

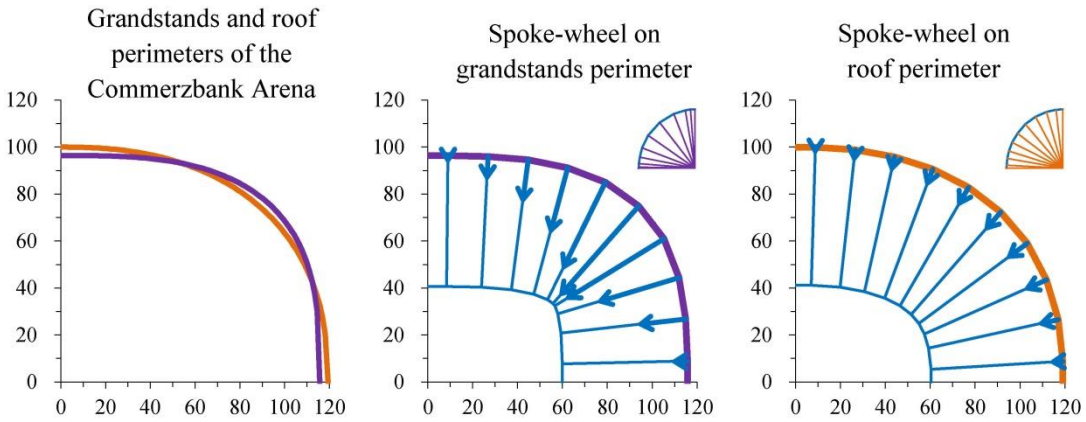

Figure 8: First quadrant of the superellipse approximating the grandstands perimeter oval (in purple) and the superellipse approximating the oval of the TSW forming the roof structure (in orange) of the Commerzbank Arena, and in-plane distribution of forces for the TSWs inscribed in the two superellipses.

2.7 Prestressing forces

In order to define the prestressing, a first situation is considered where the whole TSW shrinks homothetically in its own plane (on the left in Figure 9). Based on the (x,y) coordinates of the TSW nodes, the (x*,y*) coordinates of the same nodes in the homothetic deformation are calculated using equation (11):

$$\begin{cases} x^* = x\left(1-\dfrac{N}{E_c A_c}\right) \\ y^* = y\left(1-\dfrac{N}{E_c A_c}\right) \end{cases} \tag{11}$$

where E_c and A_c are the modulus of elasticity and the cross-sectional area of the outer polygon, respectively.

In addition to the symmetry of the spokes profile and the prestressing forces, the shortening caused by the compression force at the masts is considered negligible. Therefore, the z coordinates of the TSW nodes do not change with the deformation which is due to the prestressing forces. Equation (12) then calculates the imposed

shortening ΔL_0 that we need to introduce in each of the spoke cables and inner polygon cables for the TSW to shrink homothetically:

$$\Delta L_0 = \frac{TL}{E_t A_t} + \left(L^* - L\right) \tag{12}$$

where T is the tension force, L is the length before deformation, L^* is the length after deformation, E_t is the modulus of elasticity and A_t is the cross-sectional area of each cable.

Alternatively, to define the prestressing, a second situation can be considered in which the homothetic deformation of the outer polygon is by reduction, while the homothetic deformation of the inner polygons is by enlargement (on the right in figure 9). This is because the axial forces on the outer polygon and the axial forces on the inner polygons are of opposite sign. Then the deformation in the plane of the TSW is no longer a homothetic deformation of the original shape, but the inner and outer polygons must be deformed until the spokes are aligned with the bisectors at their vertices. So, in this case, we start with the (x^*,y^*) coordinates of the already deformed TSW and use equations (13a) and (13b) to calculate the (x,y) coordinates of the TSW before deformation. Equation (12) then calculates the imposed shortening ΔL_0 that we need to introduce in each of the cables (this time, only the spoke cables).

$$\begin{cases} x = x^* \left(1 + \dfrac{N}{E_c A_c}\right) \\ y = y^* \left(1 + \dfrac{N}{E_c A_c}\right) \end{cases}; \begin{cases} x = x^* \left(1 - \dfrac{N}{E_t A_t}\right) \\ y = y^* \left(1 - \dfrac{N}{E_t A_t}\right) \end{cases} \tag{13a and 13b}$$

In this second situation, the design of the TSW is not scalable, neither in its dimensions nor in the values of the prestressing forces. Nonetheless, it is only necessary to introduce shortenings in the spokes, which is an advantage for the assembly.

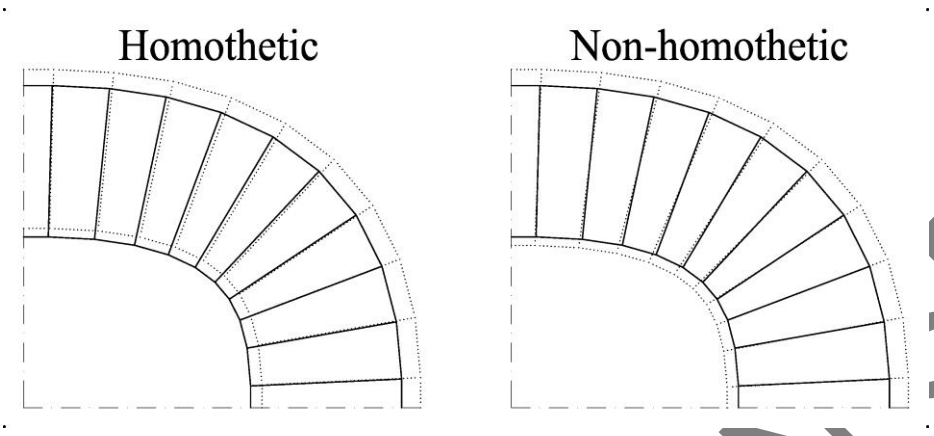

Figure 9: In-plane deformations of a TSW due to prestressing forces: homothetic deformation, introducing shortenings in the spoke cables and the inner polygon cables (on the left); and non-homothetic deformation, introducing shortenings only in the spoke cables (on the right). The dotted line represents the undeformed shape of the TSW and the solid line represents the deformed shape due to prestressing forces.

The necessary shortenings were calculated to introduce the prestressing forces in four of the TSWs defined in the previous sections, considering $q_{\max} = \pm 1$ KN/m^2, d=40 m and h_n=10 m for all wheels, and having them inscribed in four superellipses with a=100 m; the first superellipse with b=100 m and w=2, the second one with b=70 m and w=2, the third one with b=100 m and w=3, and the fourth one with b=85 m and w=2.50. The four models were analysed using *Autodesk Robot Structural Analysis* software, which provided the axial forces of the four TSWs (Figure 10). Comparing the compressive force at the outer polygon of each wheel with the compressive force of the TSW inscribed in a circumference, we can see that: in the case of the TSW with b/a=0.70 and w=2, this compression force is 1.55 times greater; in the case of the TSW with b/a=1 y w=3, it is 6.94 times greater; and in the case of the TSW with b/a=0.85 and w=2.50, it

is 3.55 times greater, as predicted by the graph in Table 5.

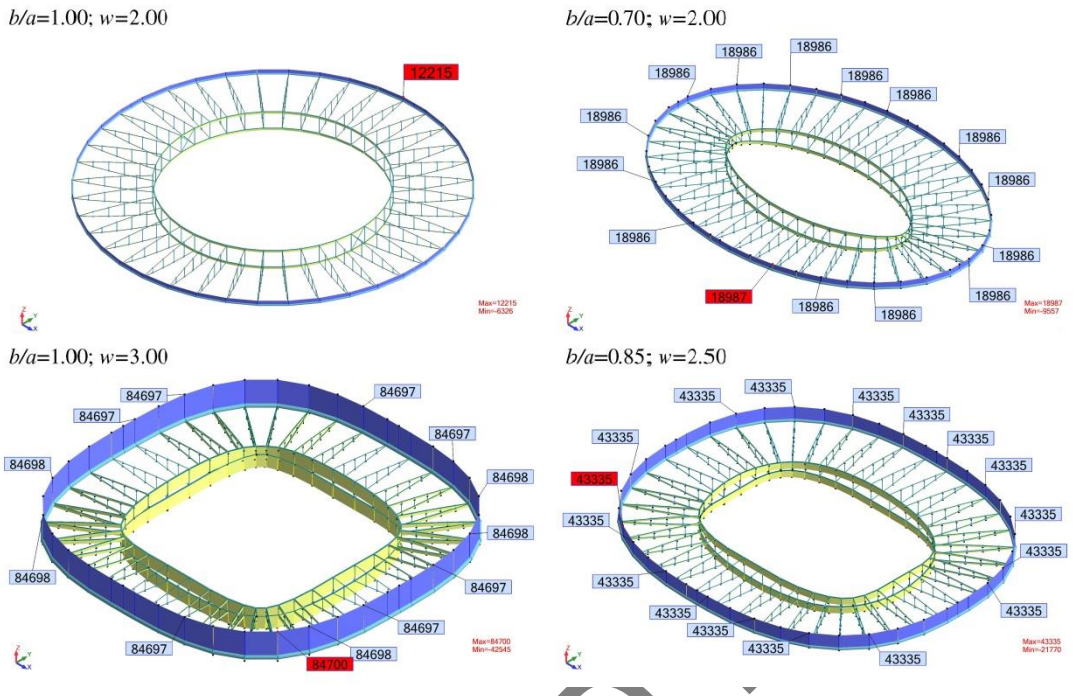

Figure 10: Diagrams of axial forces due to prestressing in four TSWs with n=10 and d=40 m, inscribed in superellipses having a=100 m; b=100 m and w=2, b=70 m and w=2, b=100 m and w=3, and b=85 m and w=2.85.

3 Conclusions

This paper presents a simplified procedure for the design and shape optimisation of a tensile spoke wheel which is inscribed in a four-centered oval or an eight-centered oval, to be used in roof structures for grandstands in sports stadiums. This procedure combines graphic static techniques with step-by-step defined numerical methods. It allows the shape of the wheel and the profile of its spokes to be determined and optimised, and the prestressing forces to be estimated.

In brief, the step by step of the procedure is as follows: First, we define a superellipse approximating a four-centred oval or an eight-centred oval by means a direct numerical method. Second, we inscribe a polygon with equal sides in a superellipse using an iterative numerical method. Third, we use graphic statics for

defining the spokes arrangement, the shape of the inner polygon and the in-plane distribution of forces. Fourth, we estimate the cross-sections of the wheel elements based on the maximum upward and downward load values and the height of the floating masts in the inner polygon. Fifth, we use graphic statics for defining the profile of the spokes and the height of the remaining floating masts. Finally, we estimate the cable shortenings required to introduce the prestressing forces.

In addition, we have included graphs to quantify the compression force on the outer polygon of a wheel which is inscribed in a superellipse, in relation to that of a circular wheel of the same size. The increase in the compression force is greater when the superellipse exponent w is greater, and smaller when the ratio b/a of the superllipse semi-axes is smaller. For example, the outer polygon of a wheel inscribed in a superellipse with $w=3$ and $b/a=0.65$ would have a compression force 13 to 14.5 times greater, depending on its depth, than that of a circular wheel of the same size.

This procedure is a tool for architects and engineers to quickly and easily obtain preliminary designs and then make minor geometric adjustments for optimisation.

Disclosure Statement

Not potential conflict of interest was reported by the authors.

Data Availability Statement

The data supporting the results of this study are available from the corresponding author upon reasonable request.

References

[1] Herrera B, Samper A. Definition and calculation of an eight-centered oval which is quasi-equivalent to the ellipse. J Geom Graph. 2015;19(2):257-268

[2] Gridgeman NT. Lamé ovals. Math Gaz. 1970:54(387): 31-37. doi: https://doi.org/10.2307/3613154.

[3] Cano A. Olympic Stadia and their architecture [dissertation]. Madrid: Universidad Politécnica de Madrid; 2016.

[4] Göppert K, Stockhusen K, Moschner T. Estádio Jornalista Màrio Filho, Rio de Janeiro. Stahlbau. 2014;83(6):368-375. doi: https://doi.org/10.1002/stab.201410163.

[5] Lombardini D, Geyer S. Cable erection of Krasnodar Stadium suspended roof. Procedia Eng. 2016;155:407-4015. doi: https://doi.org/10.1016/j.proeng.2016.08.044.

[6] Zóltowski K, Romaszkiewicz T, Drawc M. Slaski Stadium. Static and carring capacity analysis of suspension roof structure. Materialy Bodowlane. 2015. doi: https://doi.org/10.15199/33.2015.06.02.

[7] Levy MP, Jing TF. Floating saddle connections for the Georgia Dome, USA. Struct Eng Int. 1994;4(3):148-150. doi: https://doi.org/10.2749/101686694780601980.

[8] Garske E, Pravida J. Allianz Arena: Das neue Münchner Futballstadion [Allianz Arena: The new Munich football stadium]. Stahlbau. 2005;74(S1):168-178. German. doi: https://doi.org/10.1002/stab.200490275.

[9] Göppert K, Stein M. A spoked wheel structure for the world's largest convertible roof: The New Commerzbank Arena in Frankfurt, Germany. Struct Eng Int. 2007;17(4):282-287. doi: https://doi.org/10.2749/101686607782359155.

[10] Göppert K, Stockhusen K, Grotz S. Arena da Amazônia, Manaus. Stahlbau. 2014;83(6):383-389. doi: https://doi.org/10.1002/stab.201410162.

[11] Göppert K. Interdisziplinäres Entwerfen von Stadien: Unter großen Dächern [Interdisciplinary design stadiums: Under large roofs]. Bautechnik. 2012;89(10):694-700. German. doi: https://doi.org/10.1002/bate.201200049.

[12] Yao YL, Dong SL, Ma GY. Configuration, classification and development of large-span tensile cable-truss structures. Adv Mater Res. 2011;255-260:225-229. doi: https://doi.org/10.4028/www.scientific.net/AMR.255-260.225.

[13] Lachauer L, Block P. Interactive equilibrium modeling. Int J Spac Struc. 2014;29 (1):25-37. doi: https://doi.org/10.1260/0266-3511.29.1.25.

[14] Takahashi K, Ney L. Advanced form finding by constraint projections for structural equilibrium with design objectives. In: Mueller C, Adriaenssens S, editors. Creativity in Structural Design. Proceedings of IASS Annual Symposia. 2018 Jul 16-20; Boston, MA: International Journal for Shell and Spatial Structures; 2018, p. 1-8(25).

[15] Xue S, Li X, Liu Y. Advanced form finding of cable roof structures integral with supporting frames: Numerical methods and case studies. J Build Eng. 2022;60:105204. doi: https://doi.org/10.1016/j.jobe.2022.105204.

[16] Luo B, Ding MM, Han LF, et al. Structural optimization of spoke single-layer cable-net structures based on a genetic algorithm. J Aerosp Eng. 2018;31(3):04018012. doi: https://doi.org/10.1061/(ASCE)AS.1943-5525.0000831.

[17] Liu R, Cao J, Zhao H, et al. On the Plane Geometry Design Method of the Loop-free Hyperbolic Single-layer Cable Structures. KSCE J Civ Eng. 2023;27(10):4381-4391. doi: https://doi.org/10.1007/s12205-023-2382-0.

[18] Martín-Sáiz R, Herrera B. Diseño paramétrico de ruedas trianguladas de radios traccionados con perfil biconcexo para estructuras de cubierta sobre graderíos de

estadios con planta elíptica [Parametric design of triangulated tensile spoke-wheels with bi-convex profile for roof Structures on elliptical stadium stands]. Hormig Acero. 2023. Spanish. doi: https://doi.org/10.33586/hya.2023.3128.

[19] Tamai H. On a family of equilibrium geometry of a spoke-wheel system. In: Mueller C, Adriaenssens S, editors. Graphic statics. Proceedings of IASS Annual Symposia. 2018 Jul 16-20; Boston, MA: International Journal for Shell and Spatial Structures; 2018, 16, p. 1-8.

[20] Tamai H. Geometric approach to form finding of a spoke wheel system: mathematical explanations. In: Lázaro C, Bletzinger KU, Oñate E, editors. Form and Force. Proceedings of IASS Annual Symposia. 2019 Oct 7-10; Barcelona: International Association of Shell and Spatial Structures; 2019, 12, p. 1-9.

[21] Tellier X, Douthe C, Hauswirth L, et al. Funicularity of conics. Acta Mech. 2021;232:3179-3191. doi: https://doi.org/10.1007/s00707-021-02987-6.

[22] Tamai H, Takahashi K. The extended affine method for form finding of a spoke wheel system in light of graphic statics. In: Structural Morphology. Proceedings of IASS Annual Symposia. 2022; Beijing: International Association for Shell and Spatial Structures; 2022, 9, p. 1-12.

[23] Tamai H. The extended affine method for form finding of a spoke wheel system in light of graphic statics: part 2. In: Graphical Methods. Proceedings of IASS Annual Symposia. 2023; Melbourne: International Association for Shell and Spatial Structures; 2023, 16, p. 1-9.

[24] Beghini A, Beghini LL, Schultz JA, et. al. Rankine's Theorem for the design of cable structures. Struct Multidisc Optim. 2013;48:877-892. doi: https://doi.org/10.1007/s00158-013-0945-2.

[25] D'Acunto P, Jasienski JP, Ohlbrock PO, et al. Vector-based 3D graphic statics: A framework for the design of spatial structures based on the relation between form and forces. Int J Solids Struct. 2019;167:58-70. doi: https://doi.org/10.1016/j.ijsolstr.2019.02.008.

[26] Ohlbrock PO, D'Acunto. A Computer-Aided approach to equilibrium design based on graphic statics. Comput-Aided Des. 2020;121:102802. doi: https://doi.org/10.1016/j.cad.2019.102802.

[27] Standard, B. Eurocode 0 Basis of structural design—Annex A1 Application for buildings. In. BS EN, United Kingdom, 2002.

[28] Schlaich M, Liu Y, Zwingmann B. Ringseildächer mit CFK-Zugelementen [Spoke-wheel cable roof with CFRP tension members]. Bautechnik. 2014;91(10):728-741. German. doi: https://doi.org/10.1002/bate.201400031.

[29] Schlaich M, Liu Y, Zwingmann B. Carbon fiber reinforced polymer for orthogonally loaded cable net structures. 2015;25(1):34-42. doi: https://doi.org/10.2749/101686614X14043795570534.

[30] Liu Y, Zwingmann B, Shlaich M. Carbon fiber reinforced polymer for cable structures: A review. Polymers. 2015;7(10):2078-2099. doi: https://doi.org/10.3390/polym7101501.

[31] Cabello A. Predimensioning sub-space for spoke-wheel roofs. J Int Assoc Shell Spat Struct. 2018;59(2):119-130. doi: https://doi.org/10.20898/j.iass.2018.196.875.

[32] Kmet S, Kokorudova Z. Non-linear closed-form computational model of cable trusses. Int J Non-Linear Mech. 2009;44(7):735-744. doi; https://doi.org/10.1016/j.ijnonlinmec.2009.03.004.

[33] Tran HC, Lee J. Advanced form-finding for cable-strut structures. Int J Solids Sturct. 2010;47(14-15):1785-1794. doi: https://doi.org/10.1016/j.ijsolstr.2010.03.008.

List of figures